Int J Adv Manuf Technol (2018) 94:4451–4458
https://doi.org/10.1007/s00170-017-1187-z

ORIGINAL ARTICLE

Surface topography investigations on nickel alloy 625 fabricated via laser powder bed fusion

Tuğrul Özel[1] · **Ayça Altay**[1] · **Alkan Donmez**[2] · **Richard Leach**[3]

Received: 27 April 2017 / Accepted: 28 September 2017 / Published online: 4 October 2017

Abstract Laser powder bed fusion as an additive manufacturing process produces complex surface topography at multiple scales through rapid heating, melting, directional cooling, and solidification that are often governed by laser path and layer-to-layer scanning strategies and influenced by process parameters such as power, scan velocity, hatch distance, and resultant energy density. Investigations on manufactured surfaces, as-built and after applying electropolishing, are performed using stylus profilometry, digital optical microscopy, and scanning electron microscopy techniques to reveal the complex surface texture of the nickel alloy 625 test cubes that are produced by following an experimental design. Surface texture is further explored using image processing together with machine learning-based algorithms. Measurement uncertainty is also discussed briefly. The results reveal a complex nature of laser powder bed fusion created surface topography and textures as exposed with electropolishing that may further lead to a quantitative understanding of such textures and their formations influenced by different scanning strategies and process parameters.

Keywords Powder bed fusion · Surface topography · Surface texture · Nickel alloy

✉ Tuğrul Özel
ozel@rutgers.edu

[1] Industrial and Systems Engineering, Manufacturing and Automation Research Laboratory, Rutgers University, Piscataway, NJ, USA

[2] National Institute of Standards and Technology, Engineering Laboratory, Gaithersburg, MD, USA

[3] Manufacturing Metrology Team, Faculty of Engineering, University of Nottingham, Nottingham, UK

1 Introduction

The implementation of powder bed fusion (PBF)-based additive manufacturing processes in various industries for direct fabrication of metal parts with complex geometries is continuously growing [10]. Laser-based powder bed fusion (LPBF) is advantageous in obtaining fully dense three-dimensional (3D) structures without a need for post processing. LPBF typically requires high energy levels, lower scan velocities on the order of 1 m/s, and layer-to-layer rotation of scan patterns for fabricating uniformly dense parts [3, 17]. It is reported in literature that due to the high energy densities applied on the powder material with the laser beam and the related melt pool instabilities [5], material evaporation, and keyhole effects [13], the resultant structure of the fabricated 3D part, irregular microstructure [1], and subsurface integrity are some of the major concerns among other issues in laser powder bed fusion processes, especially fabricating powder nickel alloys 718 (IN718) or 625 (IN625) for mission-critical aerospace applications [4, 18].

In a PBF system, several important steps occur that affect the way the part is manufactured: (i) the part computer-aided design (CAD) geometry is oriented in the build volume and sliced into layers, (ii) the slices are then imported into a build preparation software that allows the user to specify the exact location of these slices on the substrate, (iii) a set of processing parameters (laser scan velocity, laser power, hatch spacing, etc.) are specified in the software, and (iv) laser beam path corresponding to the selected hatch pattern is generated for every layer based on the part location on the build area and the specified processing parameters.

Currently, there are no specification standards that explicitly cover measurement and characterization of surface texture for PBF metal additive manufacturing due to the unique challenges caused by the high degree of irregularity and the selection of appropriate scales of interest [16]. Understanding surface

topography and subsurface texture could help verifying the simulation work in LPBF and has the potential to optimize the related microstructure and mechanical properties [15].

The purpose of this investigation is to characterize subsurface textures resulting from various process parameter combinations. The paper describes the experimental approach, methodology to quantify the surface topography and texture characteristics (roughness of various surfaces, lay direction, fused track and melt pool marks, amount of track overlap) from contact stylus profilometry measurements, two-dimensional (2D) micrograph images, and relationships between process parameters and resulting surface characteristics.

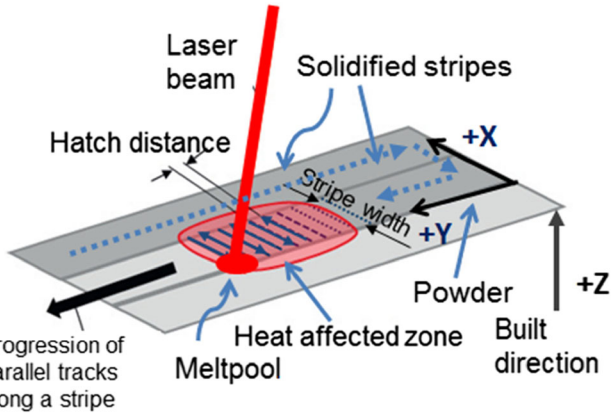

Fig. 1 Laser scanning of stripes with hatching in LPBF

2 Experimental approach

A commercial additive manufacturing grade, gas-atomized IN625 powder with average particle size of 35 μm was used as the feedstock material. Fully dense cubes (16 mm × 16 mm × 15 mm) were fabricated at the National Institute of Standards and Technology (NIST) facility using a commercial LPBF machine (EOS M270[1] Direct Metal Laser Sintering) in a nitrogen gas environment. The LPBF system consisted of a single-mode ytterbium fiber laser with a maximum power of 200 W and F-theta focusing objective that provides a spot size of approximately 100 μm. The experiments were conducted following a 3-factor, 3-level Box-Behnken design [11]. The factors and the corresponding three levels are defined as laser power (P = 169, 182, and 195 W), laser scan velocity (v_s = 725, 800, and 875 mm/s), and hatch distance (h = 0.09, 0.10, and 0.11 mm). Powder layer thickness is fixed as s = 20 μm with approximately 55% powder packing density. A minimum and a maximum energy density are obtained as 94.6 and 139.5 J/mm^3 respectively, using Eq. 1.

$$E = P/(v_s hs). \tag{1}$$

The LPBF process melts the powder and fuses desired locations on a particular layer of the powder bed. Hatching for a single layer is broken up into several "stripes" that are arranged in various patterns covering the surface (Fig. 1).

In this work, the stripes are 4 mm wide and alternate direction in a serpentine manner (as indicated with dotted lines). Each stripe consists of multiple tracks, separated by a hatch distance, and each track is processed with the laser beam moving with a constant scan velocity. After a track is completed by the movement of the laser beam in one direction, the laser turns off for approximately 0.042 ms, during which time, scanning mirrors are aligned to scan the next unprocessed track, and turns on again to move the beam in the opposite direction of the previous track. In LPBF process, scan patterns are rotated from layer to layer to obtain more uniform layer-to-layer and stripe-to-stripe fusion. Typically, scan patterns are either alternated with in orthogonal directions (i.e., 90°) or rotated about 67° from layer to layer. Therefore, two scan strategies with layer-to-layer rotation of the stripe pattern by 90° or 67° angles (scan/stripe pattern rotation, SSR) are applied in this study, as shown in Fig. 2.

The size of the molten region (melt pool) in the powder bed is influenced by process parameters, powder material properties, and process environmental effects. After a layer is finished, a new layer of powder, with a predefined thickness is placed on the powder bed. For a successful build, it is critical that the melt pool size is large enough to fuse and connect adjacent tracks and stripes in each layer and deep enough to fuse and bond with the previous layers. Inadequate or excessive energy density can easily cause incomplete fusion or extreme melting (keyhole effects) which may lead to defects in the fabricated part.

Experimental and modeling investigations of the LPBF process effects on melt pool geometry (size and shape) in multi-track processing of IN625 are presented in [6, 7]. It was identified that a dynamic melt pool geometry exists where melt pool shape and size is constantly changing along a single track during laser processing due to slight changes in energy density and the melt pool size and shape is affected by increasing energy density as it gets wider, deeper, and more asymmetrical with increasing energy density. As a result, the width of the dynamic melt pool size defines the re-solidified fused track width and the depth of the dynamic melt pool creates a fused layer together with re-melted section of the previous layer. In addition, significant powder material spatter is observed using thermal camera video monitoring as reported in [7] which leads to surface irregularities by landing of partially melted particles on solidified surfaces.

[1] Certain commercial equipment, instruments, or materials are identified in this paper in order to specify the experimental procedure adequately. Such identification is not intended to imply recommendation or endorsement by the National Institute of Standards and Technology, nor is it intended to imply that the materials or equipment identified are necessarily the best available for the purpose.

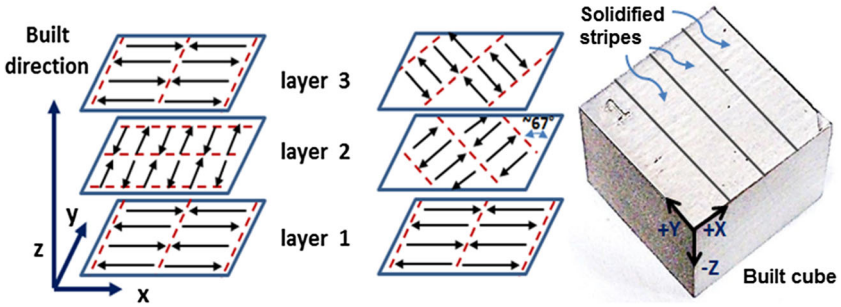

Fig. 2 Layer-by-layer rotation of stripe pattern in LPBF

Laser parameters and layerwise scan strategy have a significant influence also on the underlying microstructure of the part, which affects the resultant mechanical properties and fatigue life significantly (Amato et al. 212). Previous experimental investigations on microstructure formation on IN625 revealed LPBF process effects on growth directions of columnar grains and sizes of cellular grains as reported in [2].

This study is focused on surface texture and orientation with respect to the scan/stripe pattern rotation on the various IN625 surfaces of the test cubes obtained via the LPBF process.

3 Surface characterization

The surfaces of the nickel alloy IN625 cube analyzed include (i) as-built exposed and electropolished surface XY top, (ii) ground and electropolished surfaces (XY bottom, XZ front, YZ right), and (iii) as-built and electropolished surfaces also facing the powder in the powder bed (XZ rear, YZ left) (Fig. 3). The LPBF machine processes the XY top surface layers with the so-called "skin" parameters (P = 185 W, v_s = 800 mm/s, h = 0.05 mm) that are different from the prescribed parameters for the "core" of the part. Due to the nature of the LPBF process, the processed layers are reheated many times during the processing of new layers. The effect of reheating on the processed layers can only be observed from the interior (subsurface) surfaces.

In order to analyze the subsurface texture of LPBF processed as-built IN625 cubes shown in Fig. 3, XY bottom, XZ front, YZ right surfaces are first ground to remove approximately 500 μm from the outside surfaces using a surface grinder with SiC grinding disk in ten consecutive passes with 50 μm depth of cut per pass and about 500 m/min surface grinding velocity and about 100 mm/min feed rate. After the grinding operation, all samples were mechanically polished on SiC grit paper grade 1000. The cubes were then polished using electro-chemical polishing to reveal the texture. Electrochemical polishing was conducted in the electrolyzer and a stainless steel cathode was used. A bath containing sulfuric acid, nitric acid, and hydrofluoric acid was used. An immersion time of 1.5 h with a bath temperature heated up to 70 °C was applied to achieve uniform material removal about 50 to 60 μm on all faces of XY bottom, XZ front, YZ right.

The surfaces have been characterized with the arithmetic mean deviation *Ra* and the root mean squared deviation *Rq* (standard filtering conditions) with a Surtronic 3+ (Taylor Hobson[1]) stylus profilometer, and the morphology of the cube surfaces was investigated using a Zeiss Sigma[1] field emission scanning electron microscope (SEM) and Keyence VHX-5000[1] digital optical microscope (DOM). Field emission SEM images were obtained from the prepared test cubes using the InLens and Secondary Electron (SE2) detectors, from surfaces at multiple locations and magnification levels. Field emission SEM images of as-built sample surface facing the powder in the powder bed, as-built exposed surface XY top, a sample surface after grinding, and a sample surface after electropolishing are shown in Fig. 4.

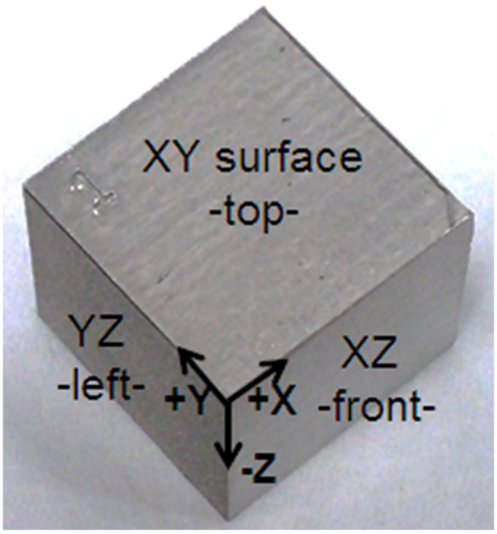

Fig. 3 Surfaces of the nickel alloy IN625 cube: XY top (as-built with skin parameters), XY bottom (ground and electropolished), XZ front (ground and electropolished), XZ rear (as-built surface facing the powder in powder bed and electropolished), YZ left (as-built surface facing the powder in powder bed and electropolished), YZ right (surface also facing the powder in powder bed electropolished)

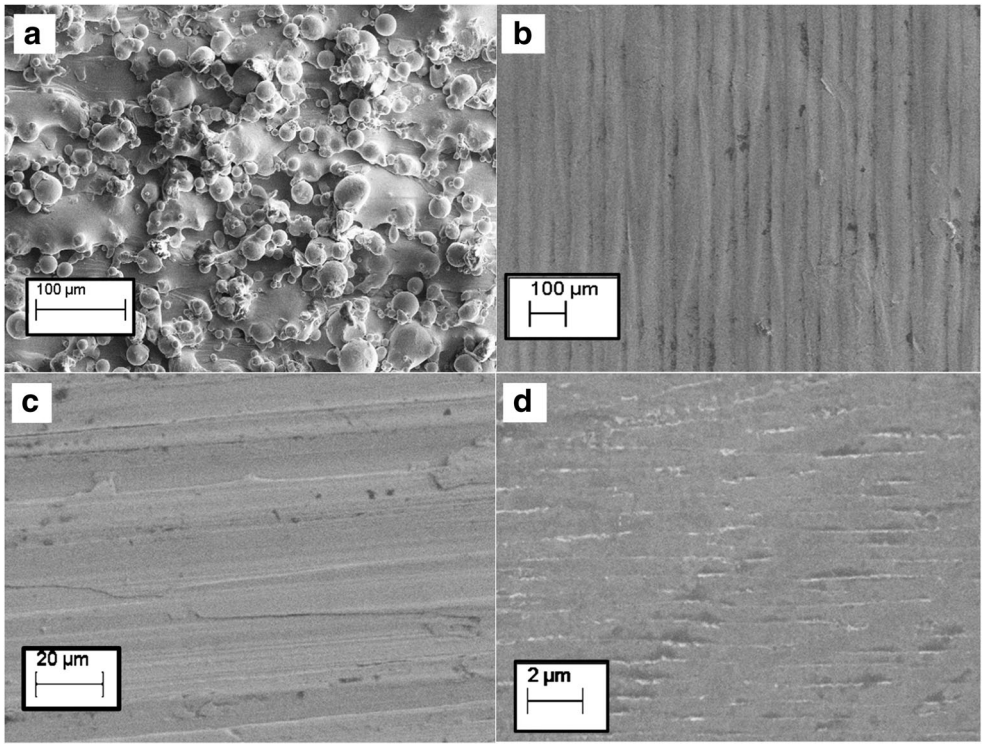

Fig. 4 Field emission SEM images of as-built surface YZ left facing the powder in the powder bed, P = 169 W, v_s = 875 mm/s, h = 0.10 mm, E = 96.57 J/mm^3, SSR = 90°, cube#1 (**a**), as-built exposed surface XY top, P = 195 W, v_s = 800 mm/s, h = 0.10 mm, E = 121.88 J/mm^3, SSR = 90°, cube#34 (**b**), surface XY bottom after grinding, P = 195 W, v_s = 800 mm/s, h = 0.10 mm, E = 121.88 J/mm^3, SSR = 90°, cube#34 (**c**), and surface XY bottom after electropolishing, P = 195 W, v_s = 800 mm/s, h = 0.10 mm, E = 121.88 J/mm^3, SSR = 90°, cube#34 (**d**)

Six built test cubes (cube#7, cube#17, cube#32, cube#34, cube#3, cube#16) have been analyzed for surface roughness under the following processing conditions: cube#7 (SSR = 67°) and cube#17 (SSR = 90°) with P = 182 W, v_s = 800 mm/s, h = 0.10 mm. Cube#32 (SSR = 67°) and cube#34 (SSR = 90°) with P = 195 W, v_s = 800 mm/s, h = 0.10 mm. Cube#3 (SSR = 67°) and cube#16 (SSR = 90°) with P = 195 W, v_s = 725 mm/s, h = 0.10 mm. The surface roughness results for averaging all measurements taken on these six cubes given in Table 1 indicate that the electropolished surfaces (Fig. 4**d**) are highly smooth and have Ra values ranging from 0.42 to 0.44 μm, and Rq values ranging from 0.60 to 0.62 μm, whereas as-built surfaces facing the powder in the powder bed (Fig. 4**a**) are highly rough and have Ra values ranging from 1.58 to 2.78 μm, and Rq values ranging from 1.76 to 3.59 μm. As-built exposed surfaces (XY top) have Ra values of 0.82 μm and Rq values of 1.10 μm. It should be noted that these surfaces are obtained using "skin" parameters of LPBF which promotes a reduction in top surface roughness with reduced hatch distance (h = 0.05 mm) and increased overlap. It was observed that the LPBF process parameters had little or no significance on the Ra values of the surfaces generated. However, there is a large standard deviation in Ra due to surface irregularities, such as sharp protrusions, recesses and open pores (as shown in Fig. 5). It should be noted that the YZ right surface (electropolished surface) has high surface roughness because it was directly electropolished without grinding retaining surface topography of as-built surface facing the powder in the powder bed.

Table 1 Surface roughness characterization of (i) as-built exposed surface XY top, (ii) electropolished surfaces (XY bottom, XZ front, YZ right), and (iii) as-built surfaces facing the powder in the powder bed (XZ rear, YZ left) of all cubes fabricated with the experimental design

Face	Ra (μm)	Std dev	Rq (μm)	Std dev
XY top	0.82	0.27	1.10	0.36
XY bottom	0.44	0.35	0.62	0.43
XZ front	0.42	0.22	0.60	0.25
XZ rear	2.78	1.28	3.59	1.60
YZ left	1.58	0.70	2.20	1.09
YZ right	1.22	0.89	1.76	1.23

A surface texture created by the fusion during LPBF process can be investigated by using DOM images obtained on the electrochemically polished XY bottom surfaces. For this purpose, DOM images were taken on the XY bottom faces of the IN625 cubes using a progressive scan DOM equipped with image sensor with an image size of 1600 (H) pixels × 1200 (V) pixels.

The texture on the electropolished surfaces is investigated by DOM of the planes that allow a cross-sectional view of XY planes. The effect of scan strategy rotation on the texture as revealed by electropolishing is shown in Fig. 6. These images are obtained from test coupons with same L-PBF process parameters but two distinct scan strategy rotations.

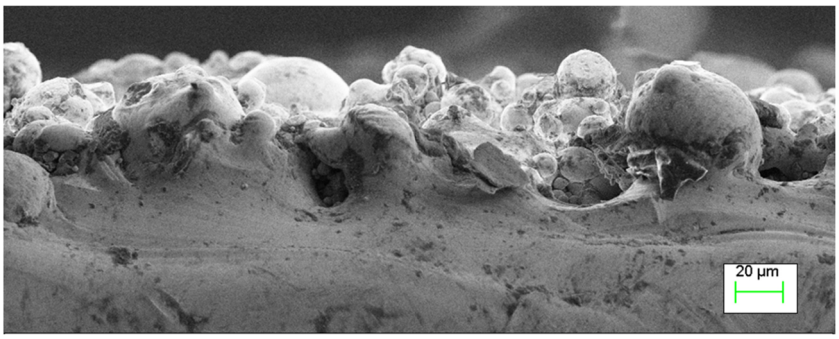

Fig. 5 Field emission SEM image of as-built surface in the powder bed indicating section with balling effect and irregularly fused surface topography (a scale bar included) (P = 195 W, v_s = 800 mm/s, h = 0.10 mm, E = 121.88 J/mm^3. SSR = 90°, cube #34)

The images reveal a surface texture with cross sections of fused tracks and layers appearing as irregular sized bands and elliptical shaped track overlaps (see Fig. 7). The fused tracks appear to be progressing in two main directions, along the scan direction and in a direction perpendicular or at an angle to the laser's scanning path. During the processing, the scanning path changes many times, thus creating fused bands (weld tracks) in different orientations. The irregular track shapes along those two directions can be explained by existence of a dynamic melt pool and fluctuating temperature gradients when large gradients of temperature or energy density concentration are present [6, 7, 18]. Also, it should be mentioned that elliptical shaped track overlaps are observed due to scan strategy rotation of layers. The fluctuations in temperature gradients and dynamic melt pool size hence fused track width seem to be increasing during laser scan processing with higher energy densities. However, we could not identify any tangible correlation between observed irregular size of fused bands and elliptical shaped track overlaps shown in Figs. 6 and 7 with laser processing parameters. These elliptical-shaped track overlaps could very well be due to the short duration direction change during tack-to-track laser processing.

In LPBF, the temperature gradient is largest in the layer-to-layer build direction (Z direction) as the cooling occurs more towards the base substrate via conduction and less so towards the ambient at the top layer [7]. There is also re-melting of the previously solidified layer of build during laser scan processing of the current layer of powder material.

In order to conduct an in-depth analysis of the effects of LPBF process parameters, the abovementioned surface characteristics, such as fused track length and width, need to be quantified. For this purpose, an image processing procedure is applied on optical 2D images by marking boundaries of the fused tracks in order to calculate the width of the fused tracks and overlapping layers and tracks commonly observed in the XY surface (Fig. 8). In Fig. 8, the boundaries of two adjacent fused tracks are illustrated together with overlapping distance.

4 Machine learning to detect the boundaries of the fused tracks

Machine learning algorithms together with image processing can be utilized to detect the boundaries of fused tracks and layers, greatly reducing the workload for manual marking of images. Feature selection is an important task in constructing machine learning algorithms, especially when a large amount of data is involved.

After various trial-and-error experiments, the best testing performance was obtained after the image was processed in the following way:

Step 1: Image de-noising using l_1 filtering is an improved version of Hodrick-Prescott (HP) filtering [9]. The

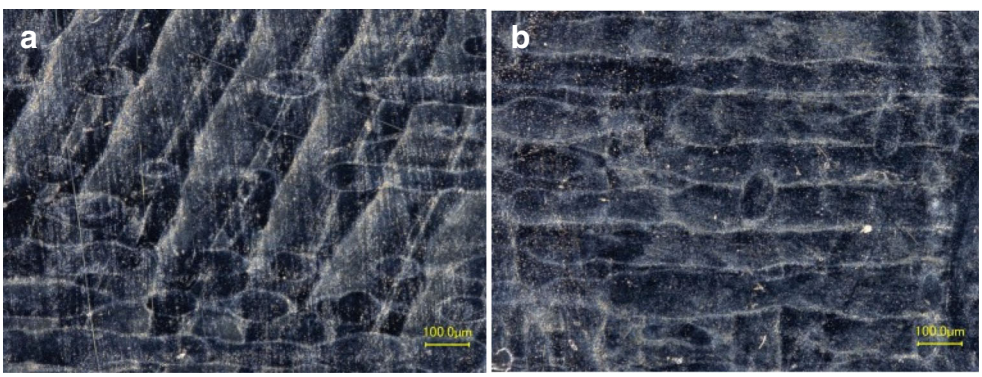

Fig. 6 Optical images of the electropolished XY surface at × 300 magnification showing a texture of fused tracks and layer-to-layer overlapping. P = 195 W, v_s = 800 mm/s, h = 0.10 mm, E = 121.88 J/mm^3. **a** SSR = 67°, cube#33, **b** SSR = 90°, cube #34

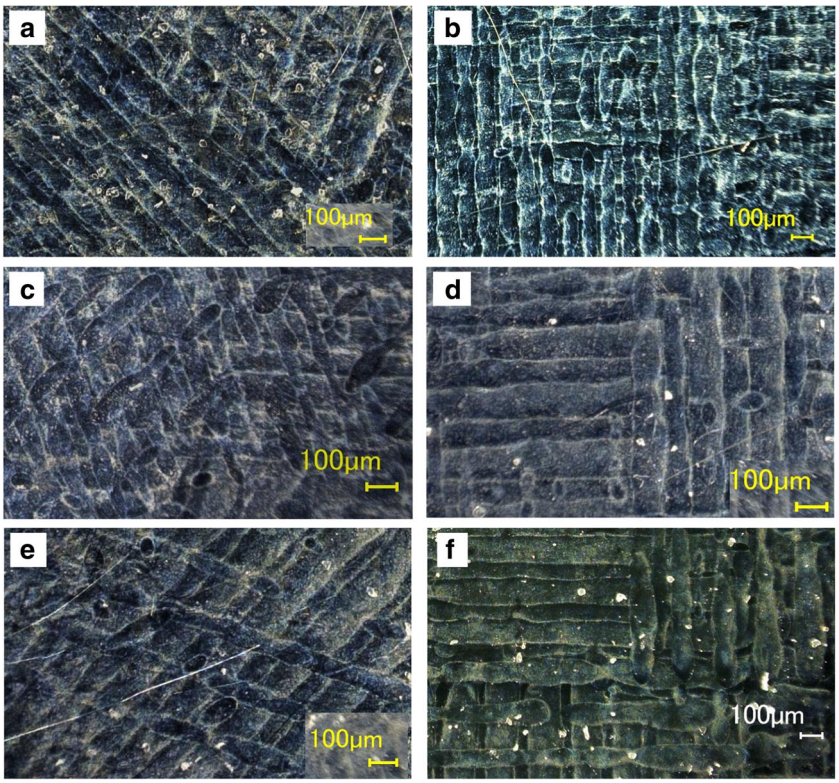

Fig. 7 Optical images of the electropolished XY surface at × 100 magnification. P = 182 W, v_s = 800 mm/s, h = 0.10 mm, E = 113.75 J/mm^3. **a** *SSR* = 67°, cube#7, **b** *SSR* = 90°, cube #17. P = 195 W, v_s = 800 mm/s, h = 0.10 mm, E = 121.88 J/mm^3. **c** *SSR* = 67°, cube#32, **d** *SSR* = 90°, cube #34. P = 195 W, v_s = 725 mm/s, h = 0.10 mm, E = 134.48 J/mm^3. **e** *SSR* = 67°, cube#3, **f** *SSR* = 90°, cube #16

implementation of l_1 filtering for image denoising is as follows [12]: Step 1.1: The red, green, and blue planes of the image are extracted separately into three data matrices R, G, B, respectively. Step 1.2. l_1 filtering is applied to each row of each matrix. Step 1.3. l_1 filtering is applied to each column of each new matrix. Step 1.4. Three matrices are united and a new image is constructed.

Step 2: Grayscale conversion has been done to all images. Each image consists of 1600 pixels × 1200 pixels, and the grayscale information of each pixel is coded as an integer between 0 to 255. Subsequently, Canny edge detection is applied on the images.

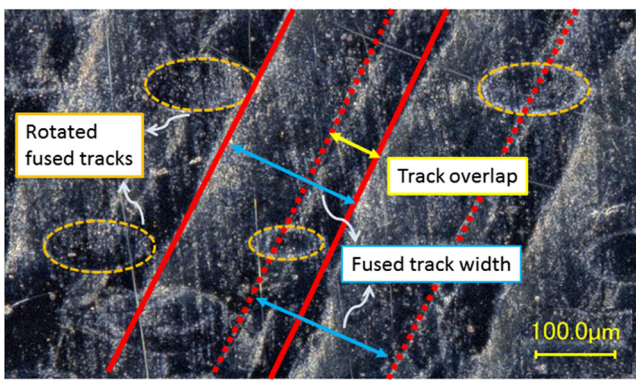

Fig. 8 Optical image of the electropolished XY surface at × 300 magnification showing fused tracks and track-to-track overlapping

Step 3: A brightness threshold is applied separately on the images. After the brightness threshold is applied, the pixels are processed with a radial filter image processing. Step 4: The resulting images are superimposed with different weights applied at each image as a coefficient for the color information. Features are then extracted from the resulting image to be used in Random Forests based classification [8] in the following manner. The eight-connected pixel neighborhood, similar to the Moore's neighborhood [14], is obtained for each pixel as shown in Fig. 9. Here, pixel $p_{i,j}$ is the central pixel, with color $c_{i,j}$.

$p_{i-1,j+1}$	$p_{i,j+1}$	$p_{i+1,j+1}$
$p_{i-1,j}$	$p_{i,j}$	$p_{i+1,j}$
$p_{i-1,j-1}$	$p_{i,j-1}$	$p_{i+1,j-1}$

Fig. 9 Eight-connected neighborhood for pixel $p_{i,j}$

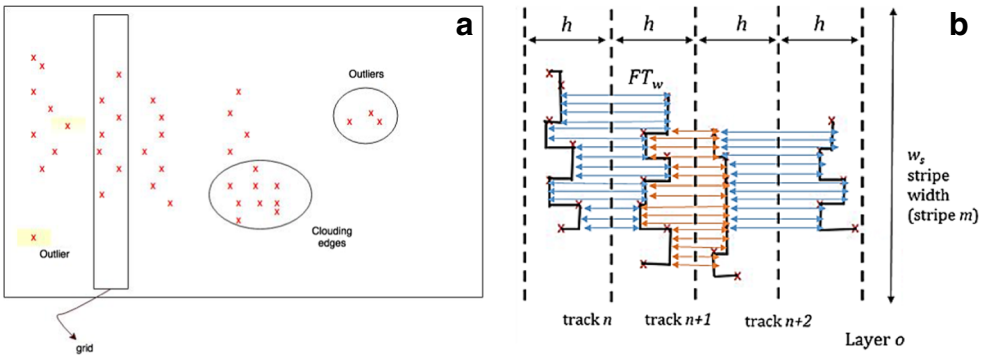

Fig. 10 Detected re-solidified melt track boundaries: **a** grid approach, **b** process signatures after the grid

Each pixel in this neighborhood is used to form a vector of features using their grayscale value, along with the central pixel. The vector is then normalized in order to improve generalization power. Additionally, the initial color of the central pixel is also included in the feature vector which is given by:

$$c = \left[\hat{c}_{i-1,j+1}\ \hat{c}_{i,j+1}\ \hat{c}_{i+1,j+1}\ \hat{c}_{i-1,j}\ \hat{c}_{i,j}\ \hat{c}_{i+1,j}\ \hat{c}_{i-1,j-1}\ \hat{c}_{i,j-1}\ \hat{c}_{i+1,j-1}\ c_{i,j}\right] \quad (2)$$

Additionally, the initial grayscale of the central pixel is also included in the feature vector. In this methodology, each pixel must have an eight-connected neighborhood; therefore, the pixels at the four edges of the original image are not treated as observations, as they do not have the required amount of neighboring pixels.

Consequently, predictions cannot be performed on the edge pixels of the image. After the input matrix is constructed, principal component analysis (PCA) is performed to further reduce the number of features. A binary output variable for each pixel is defined in the classification problem to suggest whether the pixel is on the boundary (edge) of a fused layer/track or not. This information comes from the pre-processed image (edge detection + thresholding) as explained previously. Each pixel is then treated as an observation, and subsequently, input and output matrices are constructed. A Random Forests (RF) classification model is trained with four-trees using the input matrix and the output vector defined. Finally, an image processing procedure is applied on the optical images in order to calculate the relative overlapping commonly observed in the XY cross-section of electropolished surfaces. The calculation is performed by tracing the boundaries of the overlapping fused tracks and layers on the optical images with RF-predictions first, and then calculating the relative overlapping. The edge points found can involve outliers and blurry (clouding) edges (see Fig. 10). As a result, these edge point data should be cleaned. As shown in the graph below, outlier points are pixels that do not have any connections in their close neighborhoods vertically or horizontally. Clouding edges are pixels that have multiple horizontal and vertical edge pixels, as a result, the edge boundary cannot be determined. A grid approach used to clean noisy edges. Through vertical and horizontal grids, the intensity of the edge points and their alignment is measured (Fig. 10).

All DOM images utilized for analysis were captured in 1600 pixels × 1200 pixels resolution with × 100 magnification. A built-in scale provided by the DOM was used in measuring fused weld track sizes and overlap. The number of pixels that makes up the length of the scale (100 μm) was counted to obtain a pixel-to-micrometer conversion ratio of 1.922 μm/pixel. Fused track widths and overlaps were measured by marking color-coded lines on the images and automatically counting the number of pixels spanned using machine learning. The measurements were converted to micrometers using the scale bar provided on the DOM images. The resulting length measurement standard uncertainty (Type-B) due to the subjectivity of selecting appropriate pixels defining the fused track boundaries is estimated as u_{MP} = 5 pixels × 1.922 μm/pixel = 9.61 μm by assuming a 66.67% probability that the fused track boundaries exist within 5 pixels of the points selected (2.5 pixel per boundary) [14]. In general, increasing the energy density causes an increase in the fused track width and overall overlapping of fused tracks (see Figs. 11 and 12). It should be noted that all experimental

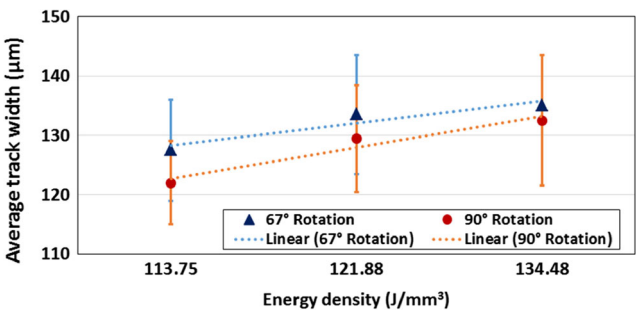

Fig. 11 Effect of energy density on the fused track width on XY surface

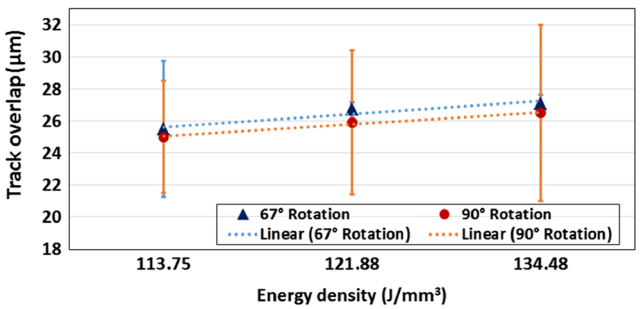

Fig. 12 Effect of energy density on the fused track overlap on XY surface

conditions given in Figs. 11 and 12 have the same hatch distance (h = 0.1 mm) and powder layer thickness (s = 20 μm). Only laser powder and scan velocity were varied to achieve three levels of energy density in each scan strategy rotation.

The error bars in these charts represent standard deviations of the fused track measurement (track width or track overlap). Stripe/scan rotation of 67° resulted in wider fused tracks albeit with significant overlapping standard deviations and larger fused track overlaps at the same energy density for all three energy density levels considered.

5 Conclusions

This study provides investigations on surface topography of as-built surfaces as well as resultant surface texture on the electropolished cross-sections of the LPBF built IN625 test cubes. Exposed fused tracks on the surface of the electropolished XY cross-sections of the test cubes were utilized to determine the texture using image processing and machine learning algorithms. The effects of energy density and stripe rotation or scan strategy on the detected surface texture for fused track widths and overlapping have been reported. The following specific conclusions are drawn from these research investigations.

- Sophisticated surface topography forms components fabricated via laser powder bed fusion process.
- As-built surfaces facing the powder in the powder bed are typically high irregular and require better definition of scale of interest.
- New methodologies are needed to quantify the surface topography and texture characteristics (roughness of various surfaces, lay direction, fused track and melt pool marks, amount of track overlap)
- Electropolished surfaces reveal fused track boundaries, tract-to-track, and layer-to-layer overlap as process signatures.
- Surface texture relationships between process parameters and resulting surface characteristics can be quantified as average track width and track-to-track overlap as related to energy density.
- Increased energy density increases track overlap and improved fusion.
- Stripe rotation or scan orientation results in wider fused tracks and larger overlaps at the same energy density.

Acknowledgements Certain commercial equipment, instruments, or materials are identified in this paper in order to specify the experimental procedure adequately. Such identification is not intended to imply recommendation or endorsement by the National Institute of Standards and Technology, nor is it intended to imply that the materials or equipment identified are necessarily the best available for the purpose.

Funding The support by the NIST under the financial assistance number 70NANB14H227 and assistances are gratefully acknowledged.

References

1. Amato KN, Gaytan SM, Murr LE, Martinez E, Shindo PW, Hernandez J, Collins S, Medina F (2012) Microstructures and mechanical behavior of Inconel 718 fabricated by selective laser melting. Acta Mater 60:2229–2239
2. Arisoy YM, Criales LE, Özel T, Lane B, Moylan S, Donmez A (2016) Influence of scan strategy and process parameters on microstructure and its optimization in additively manufactured nickel alloy 625 via laser powder bed fusion. Int J Adv Manuf Technol. https://doi.org/10.1007/s00170-016-9429-z
3. Bourell DL, Leu MC, Chakravarthy K, Guo N, Alayavalli K (2011) Graphite-based indirect laser sintered fuel cell bipolar plates containing carbon fiber additions. CIRP Ann Manuf Technol 60(1):275–278
4. Brinksmeier E, Levy G, Meyer D, Spierings AB (2010) Surface integrity of selective-laser-melted components. CIRP Ann Manuf Technol 59(1):601–606
5. Childs THC, Hauser C, Badrossamay M (2004) Mapping and modelling single scan track formation in direct metal selective laser melting. CIRP Ann Manuf Technol 53(1):191–194
6. Criales LE, Arisoy YM, Lane B, Moylan S, Donmez A, Özel T (2017a) Predictive modeling and optimization of multi-track processing for laser powder bed fusion of nickel alloy 625. Additive Manufacturing 13:14–36
7. Criales LE, Arisoy YM, Lane B, Moylan S, Donmez A, Özel T (2017b) Laser powder bed fusion of nickel alloy 625: experimental investigations of effects of process parameters on melt pool size and shape with spatter analysis. Int J Mach Tools Manuf **in press**
8. Hastie T, Tibshirani R, Friedman J (2009) The elements of statistical learning data mining, inference, and prediction. Springer-Verlag, Berlin
9. Kim SJ, Koh K, Boyd S, Gorinevsky D (2009) l_1 trend filtering. SIAM Rev 51(2):339–360
10. Kruth J-P, Levy G, Klocke F, Childs THC (2007) Consolidation phenomena in laser and powder-bed based layered manufacturing. CIRP Ann-Manuf Technol 56(2):730–759
11. NIST e-Handbook of Statistical Methods, http://www.itl.nist.gov/div898/handbook/, section 5.3.3.6.2. Dec. 23, 2016
12. Selvin S, Ajay SG, Gowri BG, Sowmya V, Somon KP (2016) l_1 trend filter for image denoising. Proc Comput Sci 93:495–502
13. Simonelli M, Tuck C, Aboulkhair NT, Maskery I, Ashcroft I, Wildman RD, Hague R (2015) A study on the laser spatter and the oxidation reactions during selective laser melting of 316L stainless steel, Al-Si10-Mg, and Ti-6Al-4V. Metall Mater Trans A 46A:3842–3851
14. Taylor BN, Kuyatt CE (1994) Guidelines for evaluating and expressing the uncertainty of nist measurement results. *NIST Technical Note 1297*. http://www.nist.gov/pml/pubs/tn1297/ Jan. 5, 2017)
15. Thompson A, Senin N, Giusca C, Leach R (2017) Topography of selectively laser melted surfaces: a comparison of different measurement methods. *CIRP Annals- Manufacturing*. Technology 66:543–546
16. Townsend A, Senin N, Blunt L, Leach RK, Taylor JS (2016) Surface texture metrology for metal additive manufacturing: a review. Precis Manuf 46:34–47
17. Yasa E, Kruth J-P, Deckers J (2011) Manufacturing by combining selective laser melting and selective laser erosion/laser re-melting. *CIRP Annals- Manufacturing*. Technology 60(1):263–266
18. Zaeh MF, Ott M (2011) Investigations on heat regulation of additive manufacturing processes for metal structures. CIRP Ann-Manuf Technol 60(1):259–262